Journal of Biomechanics 74 (2018) 116–125

Contents lists available at ScienceDirect

Journal of Biomechanics

journal homepage: www.elsevier.com/locate/jbiomech
www.JBiomech.com

Assessment of human left ventricle flow using statistical shape modelling and computational fluid dynamics

S.S. Khalafvand [a], J.D. Voorneveld [b], A. Muralidharan [a], F.J.H. Gijsen [b], J.G. Bosch [b], T. van Walsum [c], A. Haak [b], N. de Jong [b], S. Kenjeres [a,*]

[a] Department of Chemical Engineering, Faculty of Applied Science, Delft University of Technology, The Netherlands
[b] Department of Biomedical Engineering, Thorax Center, Erasmus MC, Rotterdam, The Netherlands
[c] Departments of Radiology & Nuclear Medicine and Medical Informatics, Erasmus MC, Rotterdam, The Netherlands

ARTICLE INFO

Article history:
Accepted 14 April 2018

Keywords:
Cardiac blood flow
Statistical shape modelling
Computational fluid dynamics
Left ventricle

ABSTRACT

Blood flow patterns in the human left ventricle (LV) have shown relation to cardiac health. However, most studies in the literature are limited to a few patients and results are hard to generalize. This study aims to provide a new framework to generate more generalized insights into LV blood flow as a function of changes in anatomy and wall motion. In this framework, we studied the four-dimensional blood flow in LV via computational fluid dynamics (CFD) in conjunction with a statistical shape model (SSM), built from segmented LV shapes of 150 subjects. We validated results in an in-vitro dynamic phantom via time-resolved optical particle image velocimetry (PIV) measurements. This combination of CFD and the SSM may be useful for systematically assessing blood flow patterns in the LV as a function of varying anatomy and has the potential to provide valuable data for diagnosis of LV functionality.

1. Introduction

Complex blood flow dynamics inside the heart, especially inside the left ventricle (LV), are under intensive study for potential early stage biomarkers of cardiovascular health. Of particular interest is visualization of vortex ring formation, pressure distribution, wall shear stress and energy dissipation. Several studies have shown that these indices could provide better understanding of cardiac functionality (Doenst et al., 2009; Elbaz et al., 2017; Eriksson et al., 2011; Gharib et al., 2006; Khalafvand et al., 2014; Kheradvar et al., 2012; Vasudevan et al., 2017). Imaging techniques such as magnetic resonance imaging (MRI), computed tomography (CT) and Doppler echocardiography have been used to visualize blood flow patterns and vortex ring formation in the LV (Ebbers et al., 2002; Elbaz et al., 2017; Eriksson et al., 2011; Gharib et al., 2006; Kilner et al., 2000). In addition, computational methods such as computational fluid dynamics (CFD) and fluid–structure interaction (FSI) in conjunction with MRI and CT data have been widely used to simulate and visualize patient-specific LV flow (Eriksson et al., 2011; Khalafvand et al., 2017; Khalafvand et al., 2014; Krittian et al., 2010; Long et al., 2007; Long et al., 2004; Mihalef et al., 2011; Pedrizzetti and Domenichini, 2005; Saber et al., 2003a,b; Schenkel et al., 2009; Su et al., 2016; Watanabe et al., 2004). The combination of numerical methods and imaging techniques could provide additional data for assessment of blood flow abnormality and so-called predictive medicine.

Blood flow in the LV is directly coupled to LV geometry and wall motion. Remodeling of the LV geometry may alter the blood flow patterns and hence fluid dynamics parameters such as energy dissipation (Pedrizzetti and Domenichini, 2005). Three dimensional (3D) geometric modeling of the cardiac structures is an essential prerequisite for simulations-based blood flow analysis and visualization. Such models can be obtained from patient MRI and CT images. Due to the complexity of image post-processing and computational constraints, most studies are limited to small sample sizes (Mittal et al., 2016). Blood flow analysis in a larger set of data could provide a better understanding of cardiac functionality (Biglino et al., 2016).

Abbreviations: ALE, arbitrary Lagrangian–Eulerian; CFD, computational fluid dynamics; CT, computed tomography; EDV, end-diastolic volume; EF, ejection fraction; ESV, end-systolic volume; FSI, fluid–structure interaction; LV, left ventricle; PIV, particle image velocimetry; MV, mitral valve; SI, sphericity index; SV, stroke volume; TED, time integral of energy dissipation; TRDPIV, time resolved optical particle image velocimetry; TWSS, time integral of wall shear stress; UDF, user-defined function; VFT, vortex formation time.

* Corresponding author at: Department of Chemical Engineering, Faculty of Applied Sciences, Delft University of Technology, Delft, The Netherlands.
E-mail address: s.kenjeres@tudelft.nl (S. Kenjeres).

https://doi.org/10.1016/j.jbiomech.2018.04.030
0021-9290/

Developments in imaging techniques have provided image databases and population-based studies of the heart. Statistical shape models (SSM) have been developed to parameterize the primary modes of variation observed in cardiac shapes (Biglino et al., 2016; Cootes et al., 1995; Metz et al., 2012). SSM provides a method to describe the significant shape variations of the heart geometry over a large population. SSM derived shapes, in conjunction with CFD, can be used to explore the variation of blood flow changes in a population size that would be too cumbersome to analyze on an individual basis. Additionally, analyzing these generalized shapes provides a method to obtain the relation between principal shape variations in a population and their associated hemodynamic effects. This approach may provide more general insights than when directly examining individual cases.

This study aims to quantify the characteristics of blood flow patterns in the LV using a newly developed framework. In this framework, a CFD tool is used on shapes derived from a SSM of the left heart to compute and visualize fluid dynamics characteristics of cardiac blood flow. In this study, the framework is applied on several generated shape instances, derived from the SSM that was built from the shapes of 150 subjects. Also, a shape derived from the model is physically realized by 3D printing and integrated in a dynamic in-vitro setup mimicking the beating heart. Flow in this beating heart phantom was measured using time-resolved optical particle image velocimetry (PIV) and compared with the proposed numerical CFD method.

2. Methodology

2.1. Statistical shape model (SSM)

A previously developed (Metz et al., 2012) 4-D SSM of the LV endocardium, left atrium and aorta of 150 subjects was used to generate 5 characteristic shapes. These five shapes included the mean shape, and mode variations of +3 and −3 standard deviations (SD) along the first and second principal components of shape variation in the population, representing the modes of highest energy and largest shape variation in the dataset (Fig. 1a–c). Each shape model was represented by 3D polygonal surfaces (5170 vertices) at 20 time points per cardiac cycle.

2.2. Computational fluid dynamics modelling

CFD simulation was performed with a developed semi-automatic method. For the 5 characteristic shapes from the SSM geometry reconstructed and separate unstructured grids consisting of tetrahedral cells were generated. The time resolution of the CT-derived shape model data (20 frames per cardiac cycle) was not fine enough for CFD simulation. To ensure a Courant number of less than unity (product of local fluid velocity with the ratio of time step to mesh spacing, $\frac{u\Delta t}{\Delta x} < 1$), intermediate grids were generated for each initial measurement interval between the 20 reconstructed grids from the original CT data. Approximately 2000 grids were generated during a cycle (depending on the case volume) using cubic spline interpolation. In order to solve the fluid flow domain with a finite volume method, the arbitrary Lagrangian-Eulerian (ALE) formulation of the Navier-Stokes equations was used. The integral form of the continuity equation for a volume with surface S is expressed as

$$\frac{\partial}{\partial t}\int_V \rho dV + \int_S \rho(\vec{v} - \vec{v}_b)\cdot\vec{n}\,dS = 0 \quad (1)$$

where $\vec{v}$ is the velocity vector, $\vec{v}_b$ the velocity on the boundary, $\vec{n}$ the normal vector and ρ the blood density. The momentum equation is

$$\int_V \frac{\partial}{\partial t}(\rho\vec{v})dV + \int_S \rho\vec{v}(\vec{v} - \vec{v}_b)\cdot\vec{n}\,dS = -\int_S p\mathbf{I}\cdot\vec{n}\,dS + \int_S \boldsymbol{\tau}\cdot\vec{n}\,dS \quad (2)$$

where p is the pressure, $\mathbf{I}$ the unit tensor, and $\boldsymbol{\tau}$ the viscous stress tensor. Blood flowing in the heart cavities can be treated as homogeneous Newtonian fluid with a density of 1060 kgm^{-3} and the dynamic viscosity of 0.00316 $Pa \cdot s$. This is an acceptable assumption for large vessels with inner diameter greater than approximately 0.5 mm and cardiac chambers because of relatively constant apparent viscosity of blood at high shear rates (>100/s) (Kitajima and Yoganathan, 2007). The simulation was performed in a discontinuous time step fashion during one cardiac cycle because for each time step there is a new grid (Khalafvand et al., 2017; Saber et al., 2003a; Schenkel et al., 2009). The velocity boundary conditions at mitral and aortic valve were derived from the change of LV volume (Fig. 1c). To reach a periodic solution, the simulation was repeated for four cycles and second order upwind scheme was employed. The resulting algebraic equation system was solved using the implicit PISO (Pressure Implicit with Splitting of Operators) algorithm. In this study, CFD software ANSYS FLUENT (Version 17.2) was employed to model the blood flow in LV.

The grid dependency analysis was performed to achieve the optimum grid size. Five different grids were generated: 500 K, 1 M, 2 M, 3 M and 4 M cells. An identical simulation was performed for the five model instants from SSM, and several parameters were captured to compare the results. The integral quantity of wall shear stress (WSS) over wall surfaces and the rate of energy dissipation (ED) over volumes during a cycle were calculated for all cases (Fig. 2a). The results show that the difference between 3 M and 4 M cells is less than three percent. The vortex core structure is qualitatively compared in Fig. 2b. There are no visible changes between 3 M and 4 M cells. In the present work, four million cells have been used for more accurate results, though three million cells can also capture the main flow features.

2.3. Time resolved digital PIV

To validate the numerical simulation results against a ground truth flow measurement, an experimental LV flow phantom was designed to be used for laser PIV modality (see Fig. 3). The mean SSM shape geometry at the end of systole was used as an initial geometry in the experimental setup. A compliant, optically and acoustically transparent silicone model of LV was manufactured by painting silicone (HT33 Transparente LT, ZhermackSpA, Italy) onto a mold of the LV mean shape made by 3D printing.

The silicone LV was then encased in a rigid, optically transparent acrylic box and attached to mitral and aortic valve ports fitted with Bjork-Shiley valves, which were connected to an atrial and compliance chamber, respectively. The acrylic box had one open port, which was connected to a piston pump, programmed to reciprocate in a sinusoidal pattern with a frequency of 1 Hz with 80 ml stroke volume. The box had three open surfaces for laser/-camera view access for the acquisition of laser PIV recordings. For this study degassed 66% by weight glycerol solution was used as a pumping fluid in the entire phantom. For a global overview on the experimental phantom, a movie is provided as supplementary data 1.

The velocity maps were obtained using a laser-based time-resolved optical particle image velocimetry (TRDPIV) system (LaVision Inc) as described in Table 1. Briefly, the system consists of a 150 W high speed double cavity Nd:YLF pulsed laser (operated at approximately 30 percent of its power) creating a 1 mm thick vertical illumination through the phantom, which was viewed by a high speed CMOS digital camera in planar PIV configuration. The

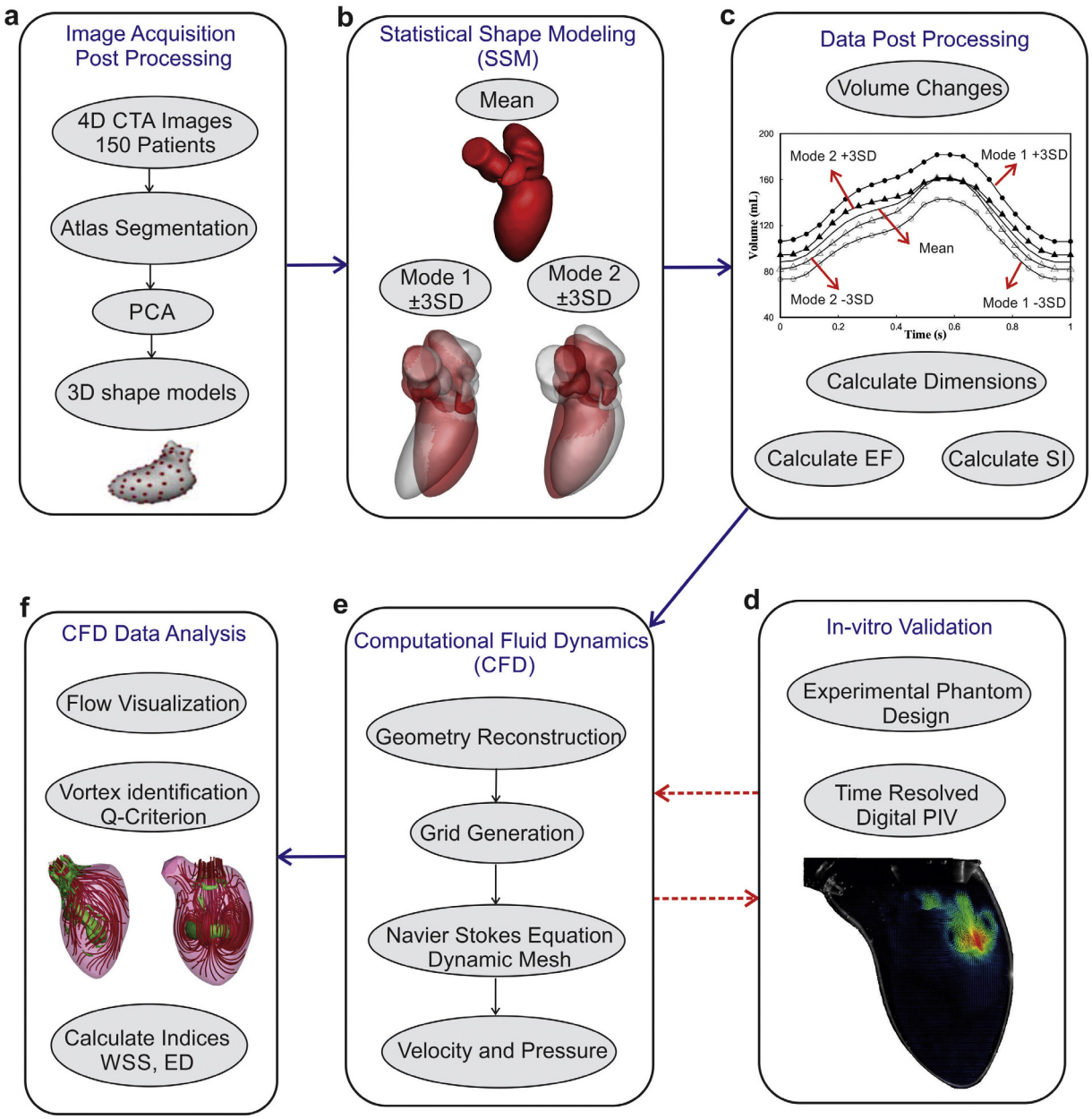

Fig. 1. The overall methodology from CT images to blood flow visualization in LV. (a) Acquisition of 4D CTA images from 150 subjects and image post-processing using multi-atlas segmentation to derive 3D shape models (Metz et al., 2012). (b) Statistical shape modeling, and generation of five characteristic 4D shapes (Metz et al., 2012). (c) Post-processing of five characteristics shapes to derive temporary change of volume during one cardiac cycle and calculate dimensions, EF and SI. (d) Experimental assessment of flow pattern using time-resolved digital PIV measurements. (e) Numerical simulation using CFD method to derive velocity and pressure distribution in LV. (f) Analysis of CFD data in LV chamber to visualize blood flow patterns and calculate numerical indices.

optical PIV receives a synchronous trigger signal from the computer controlling the piston pump. 8–12 μm Hollow glass spheres were used as seeding particles for optical PIV. The data processing was performed by DaVis 8.3 (LaVision). The velocity evaluation algorithm was a fast-Fourier transform (FFT) based cross-correlation scheme with decreasing interrogation window size ranging from 64 × 64 pixels down to 16 × 16 pixels with 50% overlap throughout. The calibrated particle images had a scaling factor of 47 μm per pixel resulting in vector maps with a grid resolution of 0.375 mm. A universal outlier detection based vector validation was utilized to remove spurious vectors and the resultant vector fields were post-processed once with a 3 × 3 denoising kernel. Finally, a temporal smoothing was applied to the vector field through a sliding averaging of 3 adjacent vector fields in time. All further processing on velocity maps was performed with custom MATLAB based programs.

2.4. Evaluation criteria

To evaluate the effects of shape changes on LV functionality, two shape-dependent indices of cardiac function are computed for the five model instances: ejection fraction (EF) and 3D sphericity index. These clinically widely used indices are based on LV volume and dimensions. Ejection fraction is defined as a percentage of blood that is pumped out of the ventricle with each contraction. The 3D sphericity index (SI) for diastole (SI-diastole) and systole (SI-systole) are calculated. The SI-diastole was defined as the ratio of the end-diastolic volume to the volume of a sphere with a diam-

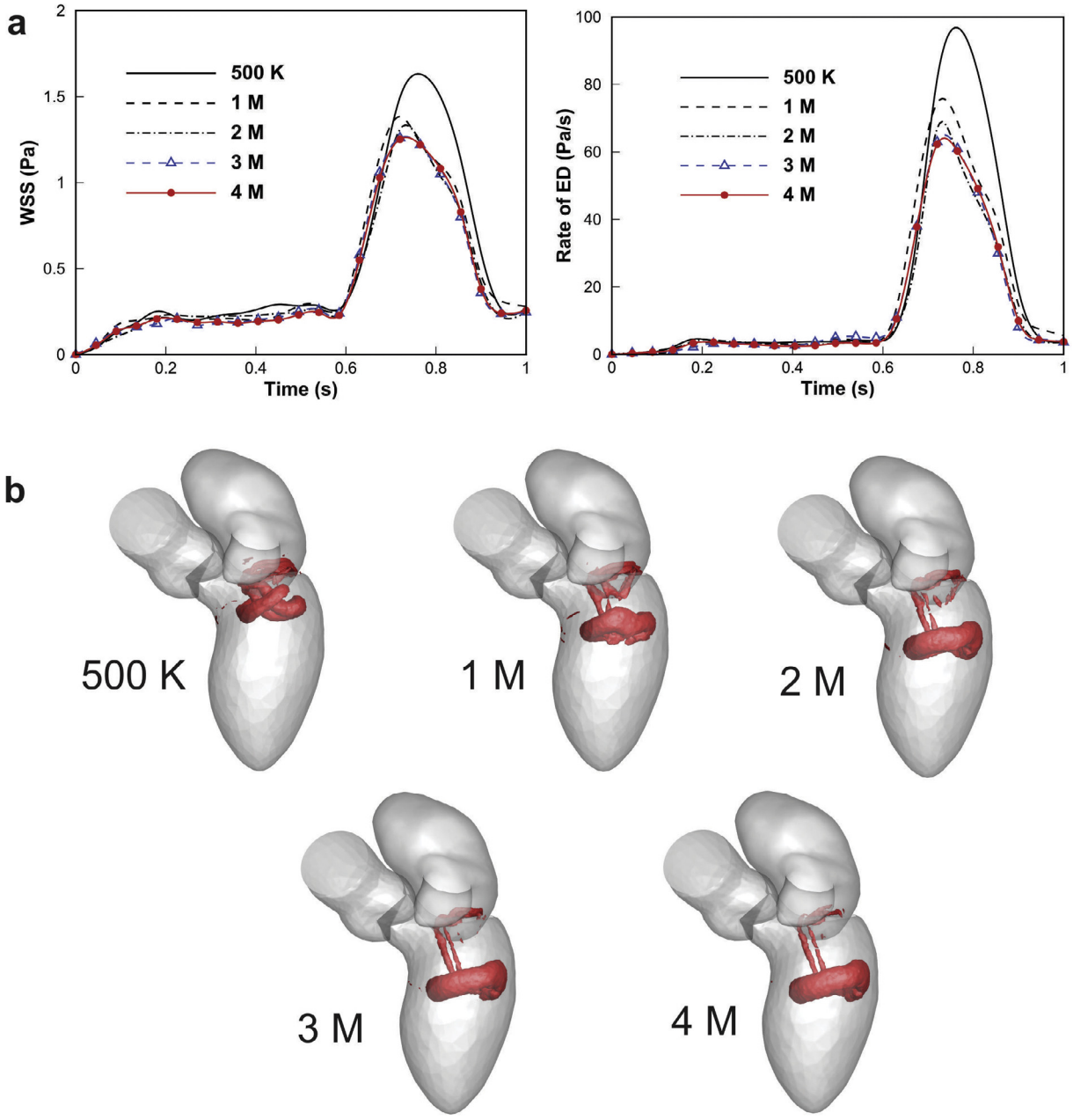

Fig. 2. Grid sensitivity analysis for five different grids (500 K, 1 M, 2 M, 3 M and 4 M cells). (a) Integral of wall shear stress (WSS) and the rate of energy dissipation (ED) during one cycle for five grids. (b) Vortex core at a time instant during the diastolic phase for five grids.

eter equal to the end-diastolic LV long axis (and similar for SI-systole) (Levine et al., 2016; Mannaerts et al., 2004). Accurate evaluation of SI is relevant for patients with myocardial infarction or implantable cardioverter-defibrillator (Levine et al., 2016; Mannaerts et al., 2004).

The 3D vortex structure was visualized by an iso-surface of the Q-criterion vortex identification (Chong et al., 1990) during diastolic and systolic phases. Q-criterion is the second invariant of the velocity gradient tensor which defines a vortex as a spatial region and can be interpreted as a relative measure of strain and the rotation rate. Aside from the qualitative analysis of flow structures, two flow criteria are computed to derive a quantitative analysis: time integrals of the energy dissipation (TED) in LV volume (Eq. (3)) and the wall shear stress (TWSS) on the LV walls (Eq. (4)), respectively. These two parameters characterize the central flow region (inside LV) and the distribution of fluid dynamic parameters on the LV wall.

$$TED = \int_0^T \left(\iiint_{LV-Volume} \mu \left(2\left(\frac{\partial u}{\partial x}\right)^2 + 2\left(\frac{\partial v}{\partial y}\right)^2 + 2\left(\frac{\partial w}{\partial z}\right)^2 + \left(\frac{\partial u}{\partial y} + \frac{\partial v}{\partial x}\right)^2 + \left(\frac{\partial u}{\partial z} + \frac{\partial w}{\partial x}\right)^2 + \left(\frac{\partial w}{\partial y} + \frac{\partial v}{\partial z}\right)^2 \right) dxdydz \right) dt \quad (3)$$

$$TWSS = \int_0^T \left(\iint_{LV-Wall} 2\mu \left(\left(\frac{\partial u}{\partial y} + \frac{\partial v}{\partial x}\right) dxdy + \left(\frac{\partial u}{\partial z} + \frac{\partial w}{\partial x}\right) dxdz + \left(\frac{\partial v}{\partial z} + \frac{\partial w}{\partial y}\right) dydz \right) \right) dt \quad (4)$$

where μ is dynamic viscosity, (u, v, w) are velocity components and T is duration of one cardiac cycle.

To quantify the duration of mitral jet into the LV, the dimensionless parameter of vortex formation time (VFT) (Gharib et al., 2006; Kheradvar et al., 2012) was used.

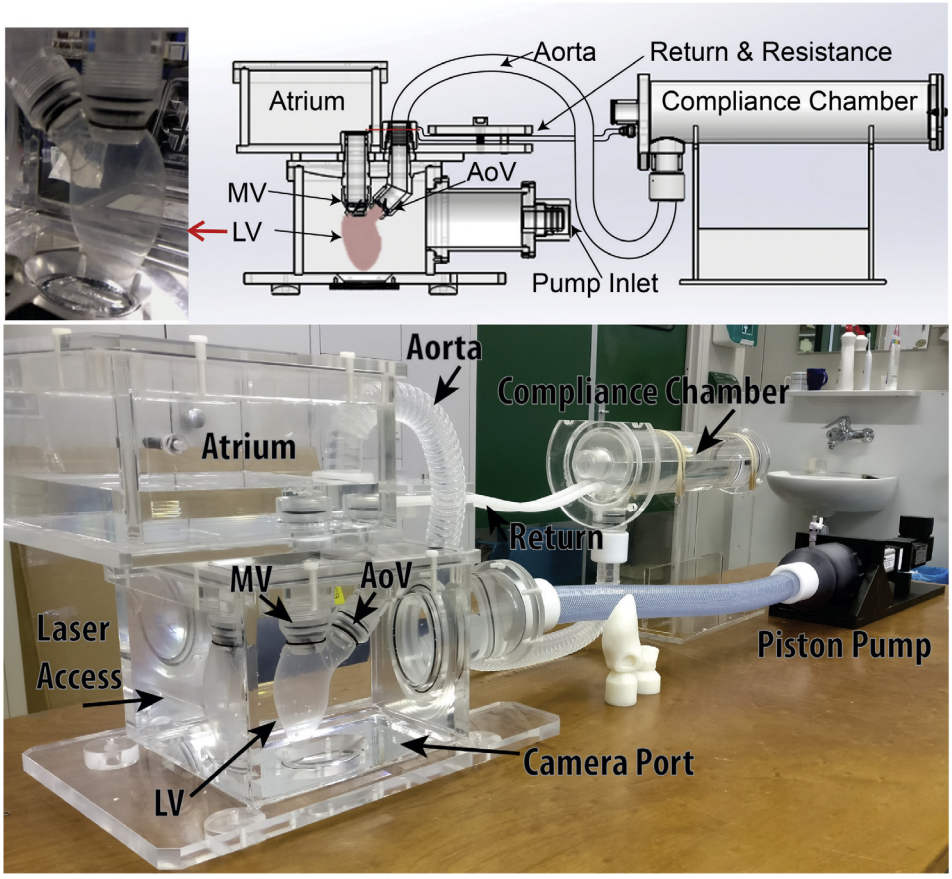

Fig. 3. Experimental LV flow phantom for laser PIV measurements. Left ventricle (LV), mitral valve (MV), aortic valve (AoV).

Table 1
Time resolved optical particle image velocimetry (TRDPIV) parameters.

Laser & illumination	150 W, 532 nm pulsed Nd:YLF Time interval: 1000 μs Illumination width: 150 ns
Camera & acquisition	2016 × 2016 pixels, 12 bit CMOS Sensor size: 11 μm Acquisition rate: 1 kHz (Single frame)
Image properties	Viewing angle: 90° (Planar PIV) Lens focal length: 100 mm Lens focal aperture: 5.6 Field of view: ~95 × 95 mm^2 Magnification: 47 μm per pixel
Particles	8–12 μm hollow glass spheres
Vector analysis	Type: Multi-pass FFT cross correlation with decreasing window size from 64 × 64 (2 pass) to 16 × 16 (5 pass) Final grid spacing: 8 pixels

$$VFT = \frac{4(1-\beta)}{\pi}\alpha^3 \times EF \text{ where } \beta = \frac{V_A}{SV} \text{ and } \alpha^3 = \frac{LVEDV}{D_E^3} \quad (5)$$

where EF is ejection fraction, V_A is the blood volume that enters LV during atrial contraction (A-wave), SV is the stroke volume, $LVEDV$ is the left ventricular end of diastole volume, and D_E is the effective diameter of the mitral geometric orifice area.

3. Results and discussion

3.1. Validation using time resolved digital PIV

Due to the sinusoidal (instead of cardiac) volume curve and elastic material of the LV, the motion of the LV phantom is different from the motion of the mean LV shape from the SSM. Further, the mechanical valve separates the inflow jet into two parts at early filling. Therefore a separate numerical simulation was performed mimicking the LV dynamics in the phantom, including valves and the viscosity of the glycerol solution. The time-dependent LV geometry and mechanical valves were reconstructed from 1000 frames (1000 fps) of experimental images. The 2D long axis contours were derived from the PIV raw images and 20 short axis cross sections were generated. To form a 3D geometry, we assumed that each short-axis cross-section is a circle. The mechanical valve is made of non-transparent material, and it is visible from the images. A video of the valve from PIV experiment is provided as supplementary data 2. The inlet and outlet boundary conditions were obtained based on PIV mean velocity at valves cross-section results.

Results are compared during early diastole, mid-diastole and initial systole (Fig. 4). The global flow patterns and velocity magnitudes are similar between PIV and CFD. During early and mid-diastole, two jets are observed in both the CFD and PIV measurements. The jets are caused by flow accelerating between the mechanical valve and outer wall. For quantitative analysis, velocity magnitudes are extracted along a line between the centers of the two main vortices during diastole and along a line between the vortex center and outlet at initial systole (white lines in Fig. 4). The results show that the PIV and CFD velocity magnitudes follow the same trends and are of comparable magnitude. A movie of velocity vectors of flow in LV measured by optical PIV is provided as supplementary data 3.

3.2. Vortex structure during diastole from CFD

Fig. 5 shows CFD results of vortex structure and velocity streamlines during diastolic phase at rapid filling (E-peak), slow filling

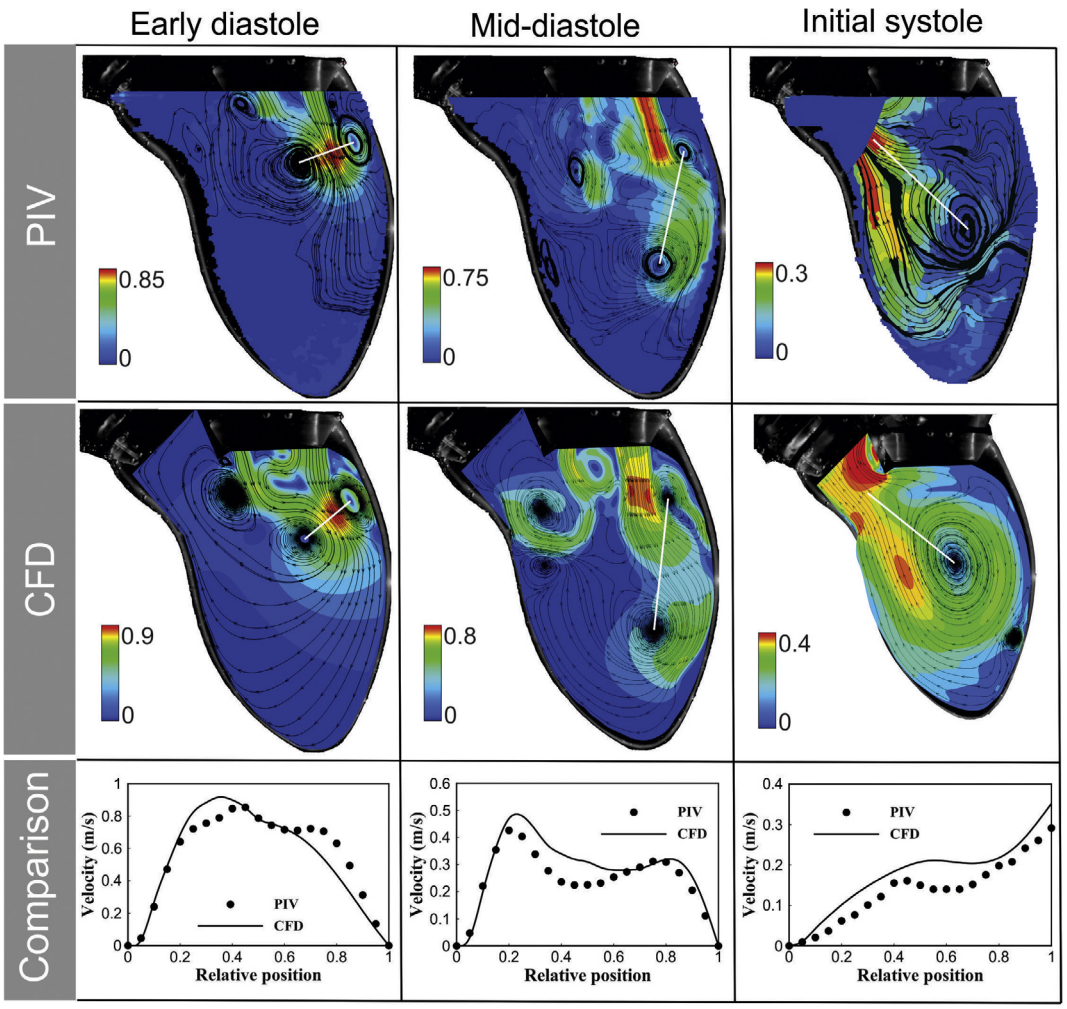

Fig. 4. Validation of numerical method using PIV. First t and second row: comparison of flow patterns between time-resolved optical PIV and CFD results for three time instances (flow patterns are colored by velocity magnitude (m/s)). Third row: comparison between velocity magnitudes extracted from white lines in the first and second row (position on line scaled from 0 to 1).

(diastasis), late filling (A-peak) and isovolumetric contraction (IVC). The accelerated flow during initial diastole results in high velocities at the aortic-mitral junction with a clockwise vortex along with a counter clockwise vortex developed on the posterior side. The vortices promptly connect forming a ring vortex which develops and travels towards the apex by the high momentum accelerating jet at the inlet. Lacking inlet momentum during diastasis, the ring vortex expands itself in LV. During late filling (second inflow jet), the primary vortex ring again moves apically, and a new vortex ring forms at the mitral annulus. At the end of the diastolic phase and IVC, vortex rings become connected and occupy the entire LV.

Vortex ring formation, movement, and direction during diastolic phase were compared between the five mode instances (Fig. 5). At rapid filling, the vortex structures present in each shape were similar. However, the vortex ring was tilted for two modes (Mode 1 −3SD and Mode 2 −3SD) due to reduced space between the aortic root and mitral annulus and wall curvature effects. During slow filling and late filling the vortex ring travels apically, but for two modes remains close to the mitral annulus (Mode 1 −3SD and Mode 2 −3SD). During IVC the difference between all modes is more obvious regarding vortex ring position and direction.

3.3. Vortex structure during systole from CFD

Fig. 6 displays systolic flow patterns at the initial stage, the peak of systole and isovolumetric relaxation (IVR). With the start of LV wall contraction, the blood is being pushed towards the aorta. At the initial stage of systole, the main vortex keeps its structure, remaining in the LV for some cases (Mode 1 +3SD, Mean and Mode 2 −3SD). As the systolic flow continues, the momentum of the fluid in the LV core region reduces, and the ring moves towards the aortic root by the LV contraction. In some cases, such as Mode 1 +3SD, Mean and Mode 2 −3SD, the vortex ring is sustained until peak systole. The overall flow pattern in the LV chamber becomes simpler with the reduction in the LV volume. Most streamlines are directed from the LV walls towards the aortic root. At the end of systole, when the outlet velocity is too low, vortices begin to develop in the LV. During IVR, the aortic valve is closed and LV chamber is suddenly motionless. This deceleration of end systole creates 3D circulatory flows (Hung et al., 2015).

For a global overview of the flow field results, a movie is provided as supplementary data 4.

3.4. Fluid dynamics and clinical criteria

TWSS, TED, and VFT over a cardiac cycle are presented in Table 2 along with EF, SI-diastole and SI-systole indices. Lower TED and TWSS means less energy loss and more efficient filling and ejection. The vortex ring during IVC will help a more efficient ejection during the initial phase of systole. The vortex can save energy and minimize energy dissipation and it can redirect flow toward aortic root during initial systole.

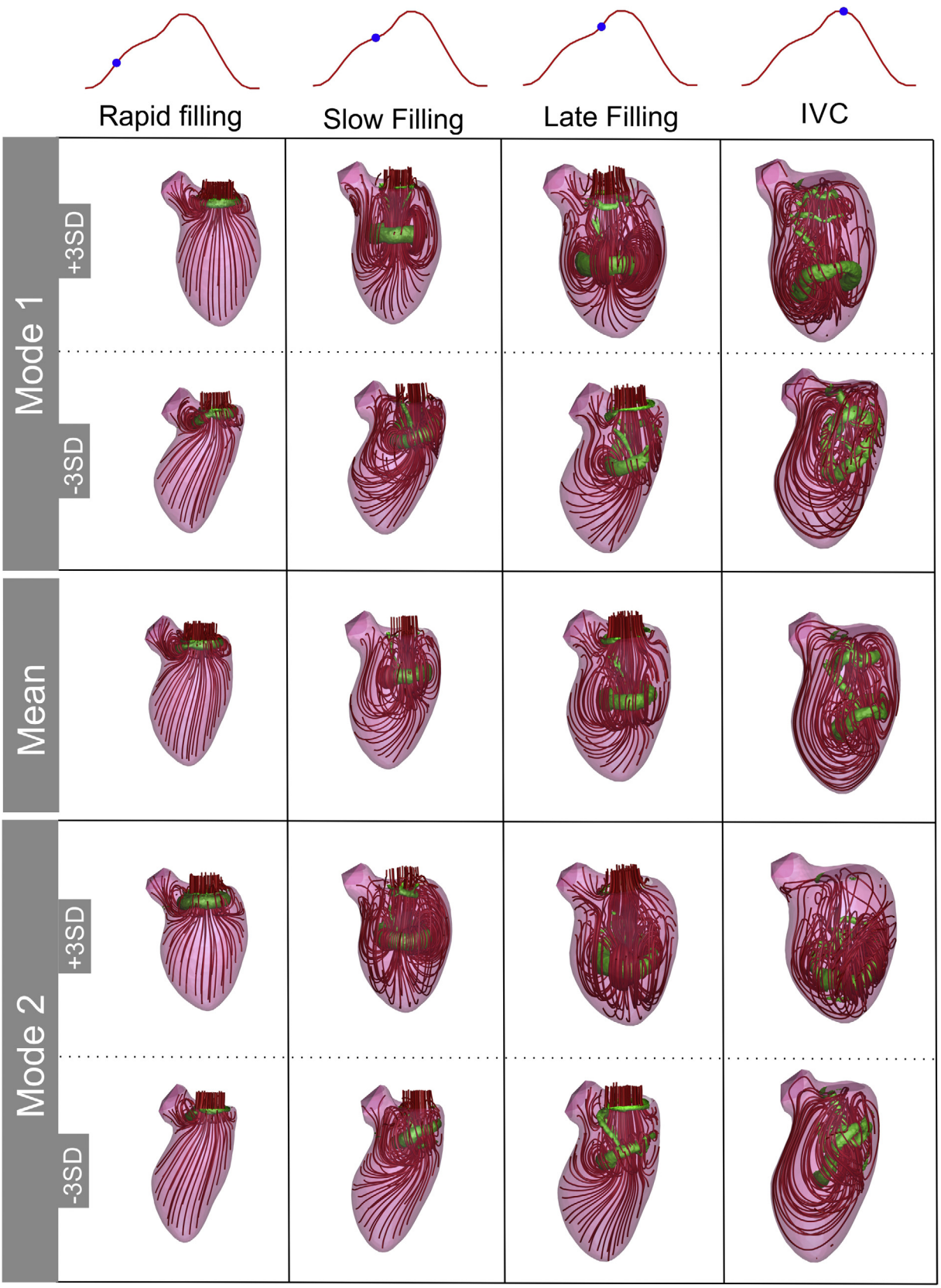

Fig. 5. Vortex structure and velocity streamlines during the diastolic phase. **Rows**, five characteristic shapes (Mode 1 ±3SD, Mean and Mode 2 ±3SD). **Columns**, four selected time steps during diastole: rapid filling or early filling (E-wave), slow filling, late filling (A-wave) and IVC. The blue point on the red line graph shows the respective time instant on the volume curve. (For interpretation of the references to color in this figure legend, the reader is referred to the web version of this article.)

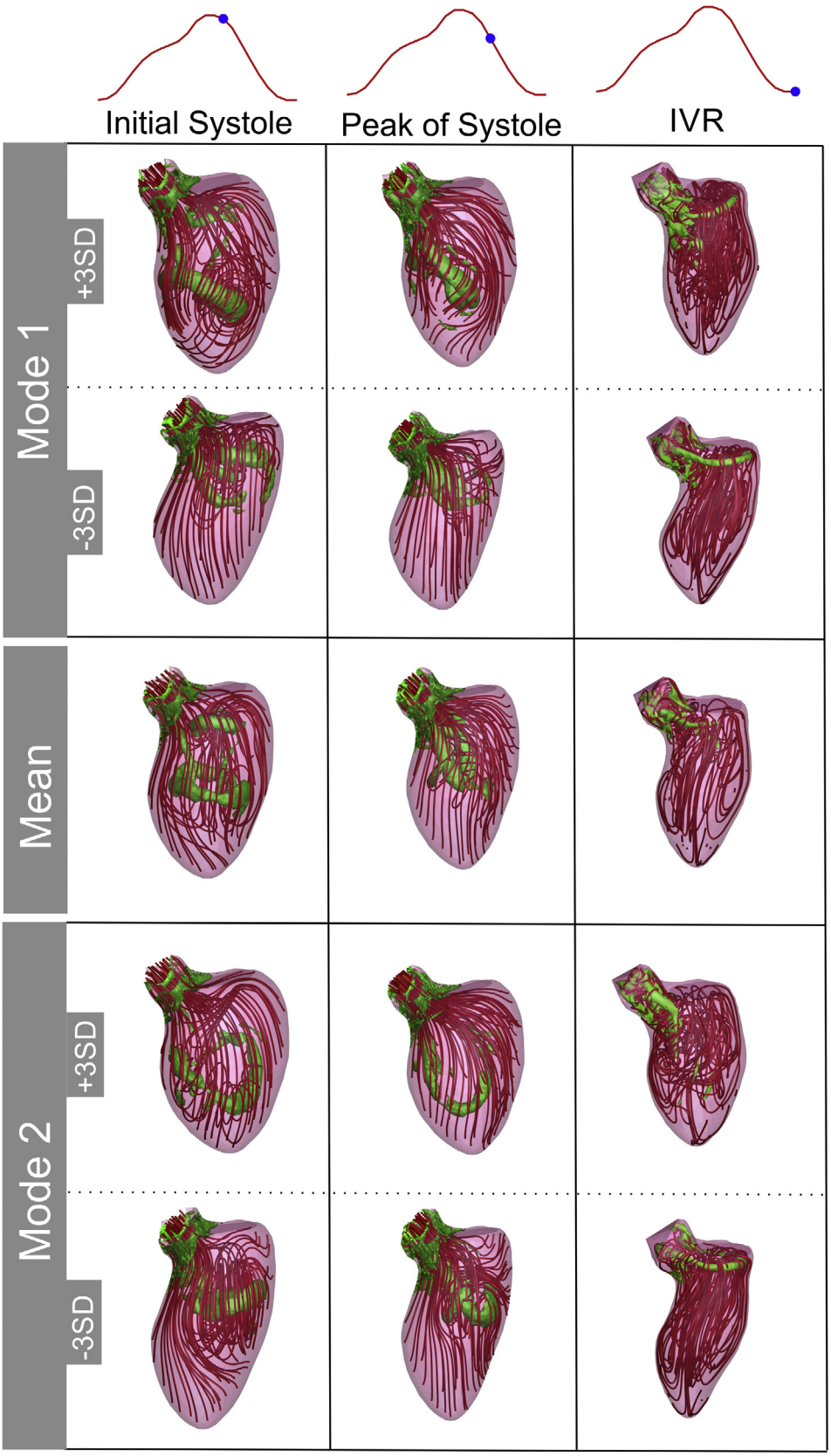

Fig. 6. Vortex structure and velocity streamlines during systolic phase**. Rows**, five characteristic shapes (Mode 1 ±3SD, Mean and Mode 2 ±3SD). **Columns**, three selected time steps during systole: initial systole, the peak of ejection and IVR. The blue point on the red line graph shows the respective time instant on the volume curve. (For interpretation of the references to color in this figure legend, the reader is referred to the web version of this article.)

Table 2
Medical and fluid dynamics parameters. Rows, five characteristic shapes (Mode 1 ±3SD, Mean and Mode 2 ±3SD). Columns, time integral of energy dissipation (TED), time integral of wall shear stress (TWSS), vortex formation time (VFT), ejection fraction (EF) and sphericity index for diastole (SI-diastole) and systole (SI-systole).

	TED (Pa)	TWSS (Pa s)	VFT	EF (%)	SI-diastole	SI-systole
Mode 1 +3SD	13.4	0.423	4.68	41.6	0.44	0.33
Mode 1 −3SD	16.7	0.464	3.12	48.8	0.40	0.30
Mean	13.6	0.417	3.86	45.3	0.42	0.32
Mode 2 +3SD	19.2	0.51	4.42	41.2	0.56	0.41
Mode 2 −3SD	13.97	0.422	3.36	49.2	0.32	0.25

The case Mode 1 +3SD has lower TED than other cases while Mode 2 +3D has the highest. This confirms the flow structure at the initial systole for these cases. The vortex ring in Mode 1 +3SD survives more than in other modes, and thus TED is less. TWSS follows the same trend as TED and Mode 2 +3SD has the highest. These results can be compared to the EF. From an EF point of view, the worst case is Mode 2 +3SD (EF = 41.2%) which corresponds to highest TED and TWSS results. From a fluid dynamics point of view, the best case is Mode 1 +3SD which has the lowest TED while its EF is very close to the worst case (41.6% vs. 41.2%). The highest EF is related to the Mode 2 −3SD while its rank is third in TED. The SI also for diastole and systole does not show a meaningful correspondence with TED except for Mode 2 +3SD which has a high SI and also high TED. These comparisons show that the EF and SI are not directly correlated to TED and TWSS.

The range of VFT for five characteristics shapes is between 3.12 and 4.68 (Table 2). In Kheradvar et al. (2012) study, the VFT was 3.8 ± 1.0 based on 45 healthy subjects, and a normal range between 3.5 and 5.5 was suggested. The VFTs in this study are in this range and can be considered as normal subjects. Poh et al. (2012) compared control subjects and heart failure patients with preserved EF, and the VFTs were 2.67 ± 0.80 and 2.21 ± 0.80, respectively. Although their method of calculating VFT was different from the original definition in Gharib et al. (2006), their study clearly demonstrated that the VFT is not the only decisive factor. In this study, there is no meaningful correlation between VFT and other parameters.

3.5. Limitations

Despite aforementioned advantages of our framework, it also suffers from limitations. The results are validated using planar two component PIV instead of the 3D three-component PIV. Both mitral and aortic valves are modeled as an orifice, and papillary muscles inside the LV are ignored. The mitral valve plays an important role in the LV flow (Khalafvand et al., 2015; Seo et al., 2014; Vedula et al., 2015). However, due to imaging limitation to capture mitral valve movement in a large number of patients (150 cases), mitral valve was excluded in this study. Although we have used high order numerical schemes and fine grids, numerical errors can affect the results.

We used the framework to simulate mean and two selected modes of variation of the shape model and its impact on the blood flow patterns. However, the modes are not related to diseases because the clinical data on the patients are not available. The shape modes of variation can present a different type of diseases and can be used to develop devices that fit the majority or different classes of populations (Biglino et al., 2016).

4. Conclusion and outlook

In this study, a new framework is presented to simulate, visualize and analyze blood flow in LV. Five characteristic 4D shapes (Mean, Mode 1 ±3SD and Mode 2 ±3SD) of 150 subjects are derived from SSM to cover generalized LV shape changes. Using these shape instances, CFD simulations are performed to explore the effects of shape changes on blood flow dynamics in the LV. The results are validated in an in-vitro dynamic setup via time-resolved optical PIV measurements. For quantitative evaluation, we calculated the TED, TWSS and VFT as well as EF and SI. Comparison between model instances shows that TED and TWSS are minimized for three model instances (Mode 1 +3SD, Mean and Mode 2 −3SD) and the ring vortex persist more than other cases during systole. This indicates that there might be added value to determine both geometrical and fluid dynamic indices.

The proposed framework enables to gain more insight into LV shape differences between healthy subjects and patients. To investigate how shape affects function and ultimately patient outcome, this framework can be useful. To develop the current framework, obtaining clinical data of the patients is needed. Applying current framework on a large number of patients with different type of diseases and dividing patients based on type of disease to shape subgroups could explore if any of those subgroups are at a higher risk and even inspire novel surgical approaches for repairing specific morphologies.

Acknowledgments

This research is founded by The Netherlands Organization for Health Research and Development (ZonMW), within the project “4D Flow and Heart Failure”, number 104003001.

Conflict of interest statement

The authors declare that they have no conflict of interest in regards to this study.

Appendix A. Supplementary material

1. A movie of experimental setup for PIV measurements in LV model.
2. A movie of velocity vectors of flow in LV measured by optical PIV.
3. A movie of velocity streamlines, shear stress and vortex structure during one cardiac cycle for the mean shape.

Supplementary data associated with this article can be found, in the online version, at https://doi.org/10.1016/j.jbiomech.2018.04.030.

References

Biglino, G., Capelli, C., Bruse, J., Bosi, G.M., Taylor, A.M., Schievano, S., 2016. Computational modelling for congenital heart disease: how far are we from clinical translation? Heart.
Chong, M.S., Perry, A.E., Cantwell, B.J., 1990. A general classification of three-dimensional flow fields. Phys. Fluids A 2, 765–777.
Cootes, T.F., Taylor, C.J., Cooper, D.H., Graham, J., 1995. Active shape models-their training and application. Comput. Vis. Image Underst. 61, 38–59.
Doenst, T., Spiegel, K., Reik, M., Markl, M., Hennig, J., Nitzsche, S., Beyersdorf, F., Oertel, H., 2009. Fluid-dynamic modeling of the human left ventricle:

methodology and application to surgical ventricular reconstruction. Ann. Thoracic Surgery 87, 1187–1195.
Ebbers, T., Wigström, L., Bolger, A.F., Wranne, B., Karlsson, M., 2002. Noninvasive measurement of time-varying three-dimensional relative pressure fields within the human heart. J. Biomech. Eng. 124, 288–293.
Elbaz, M.S.M., van der Geest, R.J., Calkoen, E.E., de Roos, A., Lelieveldt, B.P.F., Roest, A. A.W., Westenberg, J.J.M., 2017. Assessment of viscous energy loss and the association with three-dimensional vortex ring formation in left ventricular inflow: In vivo evaluation using four-dimensional flow MRI. Magn. Reson. Med. 77, 794–805.
Eriksson, J., Dyverfeldt, P., Engvall, J., Bolger, A.F., Ebbers, T., Carlhäll, C.J., 2011. Quantification of presystolic blood flow organization and energetics in the human left ventricle. Am. J. Physiol. – Heart Circulat. Physiol. 300, H2135.
Gharib, M., Rambod, E., Kheradvar, A., Sahn, D.J., Dabiri, J.O., 2006. Optimal vortex formation as an index of cardiac health. Proc. Natl. Acad. Sci. 103, 6305–6308.
Hung, T.-K., Khalafvand, S.S., Ng, E.Y.-K., 2015. Fluid dynamic characteristics of systolic blood flow of the left ventricle. J. Mech. Med. Biol. 15, 1550047.
Khalafvand, S.S., Hung, T.-K., Ng, E.Y.-K., Zhong, L., 2015. Kinematic, dynamic, and energy characteristics of diastolic flow in the left ventricle. Comput. Math. Methods Med. 2015, 12.
Khalafvand, S.S., Ng, E.Y.-K., Zhong, L., Hung, T.-K., 2017. Three-dimensional diastolic blood flow in the left ventricle. J. Biomech. 50, 71–76.
Khalafvand, S.S., Zhong, L., Ng, E.Y.K., 2014. Three-dimensional CFD/MRI modeling reveals that ventricular surgical restoration improves ventricular function by modifying intraventricular blood flow. Int. J. Num. Methods Biomed. Eng. 30, 1044–1056.
Kheradvar, A., Assadi, R., Falahatpisheh, A., Sengupta, P.P., 2012. Assessment of transmitral vortex formation in patients with diastolic dysfunction. J. Am. Soc. Echocardiogr. 25, 220–227.
Kilner, P.J., Yang, G.-Z., Wilkes, A.J., Mohiaddin, R.H., Firmin, D.N., Yacoub, M.H., 2000. Asymmetric redirection of flow through the heart. Nature 404, 759–761.
Kitajima, H., Yoganathan, A.P., 2007. Blood Flow—The Basics of the Discipline, Ventricular Function and Blood Flow in Congenital Heart Disease. Blackwell Publishing, pp. 38–54.
Krittian, S., Janoske, U., Oertel, H., Böhlke, T., 2010. Partitioned fluid-solid coupling for cardiovascular blood flow. Ann. Biomed. Eng. 38, 1426–1441.
Levine, Y.C., Matos, J., Rosenberg, M.A., Manning, W.J., Josephson, M.E., Buxton, A.E., 2016. Left ventricular sphericity independently predicts appropriate implantable cardioverter-defibrillator therapy. Heart Rhythm 13, 490–497.
Long, Q., Merrifield, R., Xu, X.Y., Kilner, P., Firmin, D.N., Yang, G.Z., 2007. Subject-specific computational simulation of the left ventricular flow based on magnetic resonance imaging. Proc. Inst. Mech. Eng. H 222.
Long, Q., Merrifield, R., Yang, G.Z., Xu, X.Y., Kilner, P.J., Firmin, D.N., 2004. The influence of inflow boundary conditions on intra left ventricle flow predictions. J. Biomech. Eng. 125, 922–927.
Mannaerts, H.F.J., van der Heide, J.A., Kamp, O., Stoel, M.G., Twisk, J., Visser, C.A., 2004. Early identification of left ventricular remodelling after myocardial infarction, assessed by transthoracic 3D echocardiography. Eur. Heart J. 25, 680.
Metz, C.T., Baka, N., Kirisli, H., Schaap, M., Klein, S., Neefjes, L.A., Mollet, N.R., Lelieveldt, B., Bruijne, M.D., Niessen, W.J., Walsum, T.V., 2012. . Regression-based cardiac motion prediction from single-phase CTA. IEEE Trans. Med. Imag. 31, 1311–1325.
Mihalef, V., Ionasec, R.I., Sharma, P., Georgescu, B., Voigt, I., Suehling, M., Comaniciu, D., 2011. Patient-specific modelling of whole heart anatomy, dynamics and haemodynamics from four-dimensional cardiac CT images. Interface Focus 1, 286.
Mittal, R., Seo, J.H., Vedula, V., Choi, Y.J., Liu, H., Huang, H.H., Jain, S., Younes, L., Abraham, T., George, R.T., 2016. Computational modeling of cardiac hemodynamics: Current status and future outlook. J. Comput. Phys. 305, 1065–1082.
Pedrizzetti, G., Domenichini, F., 2005. Nature optimizes the swirling flow in the human left ventricle. Phys. Rev. Lett. 95, 108101.
Poh, K.K., Lee, L.C., Shen, L., Chong, E., Tan, Y.L., Chai, P., Yeo, T.C., Wood, M.J., 2012. Left ventricular fluid dynamics in heart failure: echocardiographic measurement and utilities of vortex formation time. Eur. Heart J. – Cardiovascul. Imag. 13, 385–393.
Saber, N.R., Wood, N.B., Gosman, A.D., Merrifield, R.D., Yang, G.-Z., Charrier, C.L., Gatehouse, P.D., Firmin, D.N., 2003a. Progress towards patient-specific computational flow modeling of the left heart via combination of magnetic resonance imaging with computational fluid dynamics. Ann. Biomed. Eng. 31, 42–52.
Saber, N.R., Wood, N.B., Gosman, A.D., Merrifield, R.D., Yang, G.Z., Charrier, C.L., Gatehouse, P.D., Firmin, D.N., 2003b. Progress towards patient-specific computational flow modeling of the left heart via combination of MRI with CFD. Ann. Biomed. Eng. 31.
Schenkel, T., Malve, M., Reik, M., Markl, M., Jung, B., Oertel, H., 2009. MRI-Based CFD analysis of flow in a human left ventricle: methodology and application to a healthy heart. Ann. Biomed. Eng. 37, 503–515.
Seo, J.H., Vedula, V., Abraham, T., Lardo, A.C., Dawoud, F., Luo, H., Mittal, R., 2014. Effect of the mitral valve on diastolic flow patterns. Phys Fluids 26.
Su, B., Tan, R.S., Tan, J.L., Guo, K.W.Q., Zhang, J.M., Leng, S., Zhao, X., Allen, J.C., Zhong, L., 2016. Cardiac MRI based numerical modeling of left ventricular fluid dynamics with mitral valve incorporated. J. Biomech. 49, 1199–1205.
Vasudevan, V., Low, A.J.J., Annamalai, S.P., Sampath, S., Poh, K.K., Totman, T., Mazlan, M., Croft, G., Richards, A.M., de Kleijn, D.P.V., Chin, C.-L., Yap, C.H., 2017. Flow dynamics and energy efficiency of flow in the left ventricle during myocardial infarction. Biomech. Model. Mechanobiol., 1–15
Vedula, V., Seo, J.H., Lardo, A.C., Mittal, R., 2015. Effect of the trabeculae and papillary muscles on the hemodynamics of the left ventricle. Theor. Comp. Fluid. Dyn.
Watanabe, H., Sugiura, S., Kafuku, H., Hisada, T., 2004. Multiphysics simulation of left ventricular filling dynamics using fluid-structure interaction finite element method. Biophys. J. 87, 2074–2085.